Nanoscale Advances

ROYAL SOCIETY OF CHEMISTRY

PAPER

View Article Online
View Journal | View Issue

Check for updates

Cite this: *Nanoscale Adv.*, 2026, **8**, 912

Dual functionality of silver- and bismuth-based molybdenum disulfide multiple phases towards effective oxygen evolution reaction and dye degradation

Asma Asmat,[a] Sobia Dilpazir,[a] Muhammd Imran,*[b] Sawaira Moeen,[c] Anwar Ul-Hamid,[d] Ghafar Ali[e] and Muhammad Ikram*[c]

Received 10th August 2025
Accepted 17th November 2025

DOI: 10.1039/d5na00763a

rsc.li/nanoscale-advances

The engineering of two-dimensional (2D) layered materials through metallic and non-metallic doping has proven to be an intriguing strategy for achieving efficient water oxidation and high catalytic activities. The current study reveals the fabrication of a novel bifunctional Ag/Bi-doped MoS_2 catalyst with a fixed concentration (2 wt%) of bismuth (Bi) and varying concentrations (1 and 3 wt%) of silver (Ag) as dopants in MoS_2 (host) using a facile hydrothermal strategy. The Bi-doped MoS_2 catalyst with 3 wt% Ag exhibited an excellent catalytic activity of 99.57% for the elimination of RhB dye from water and flexibility in a wide pH range, signifying its catalytic dye-degradation potential in diverse pH environments. Additionally, the bifunctional catalyst demonstrated an outstanding electrocatalytic OER performance, requiring an overpotential of only 192 mV to reach a current density of 10 mA cm^{-2} and a small Tafel slope of 65.3 mV dec^{-1}.

1. Introduction

Water is a basic element for the survival and growth of humans and other living beings.[1] Despite the abundance (71%) of water on the Earth's crust, only 0.03% is acceptable for human consumption.[2] Water reservoirs are frequently contaminated by wastewater coming from textile, paper, petroleum and leather industries, containing large amounts of dyes in it.[3] Methyl orange (MO), rhodamine B (RhB) and methylene blue (MB) are some common organic dyes discharged from industries, posing detrimental effects on human health and the environment.[4] In recent decades, a variety of techniques have been implemented to reduce dye content in wastewater, for instance, coagulation, filtration, catalytic degradation, photocatalysis, adsorption, and biodegradation.[5] Among these, the catalytic degradation using 2D materials is an effective renewable approach for the reduction of harmful dyes and other pollutants from water.[6]

Another major problem encountered by the modern world is a severe energy crisis owing to the widespread depletion of energy resources.[7] Various countries have predominantly relied on fossil fuels to meet the growing energy demands.[8] This extensive utilization of fossil fuels has led to their depletion, degraded the natural environment, and disturbed the ecological balance.[9] The prime concern is to explore alternative sources of energy that are sustainable and eco-friendly.[10] Hydrogen has been proposed as a good alternative to non-renewable energy sources.[11,12]

One of the defining factors in promoting a hydrogen-based economy is its contribution to reducing carbon emissions into the environment.[13] Currently, about 95% of industrial hydrogen production primarily relies on the steam methane reforming method, releasing around 830 million tons of CO_2 annually.[14] Therefore, there is a continuous need to develop green and sustainable methods to generate hydrogen as a clean energy carrier.[15] Electrochemical water splitting is a sustainable and economical approach to producing carbon-free hydrogen fuel.[16] It is a process that requires a standard theoretical potential of 1.23 V to split water into H_2 and O_2.[17] Two distinct half-reactions, the cathodic hydrogen evolution reaction (HER) and anodic oxygen evolution reaction (OER), constitute the thorough process of electrochemical water splitting.[18,19] However, a multistep electron transfer, particularly in the OER, results in slow reaction kinetics and substantial energy loss during the reaction, declining the overall efficiency of energy conversion.[20,21]

---

[a] *Department of Chemistry, Comsats University, Islamabad 45550, Pakistan*

[b] *Interdisciplinary Research Center for Hydrogen Technologies and Carbon Management (IRC-HTCM), King Fahd University of Petroleum & Minerals, Dhahran 31261, Saudi Arabia. E-mail: muhammad.imran@kfupm.edu.sa*

[c] *Solar Cell Applications Research Lab, Department of Physics, Government College University Lahore, Lahore, Punjab, 54000, Pakistan. E-mail: dr.muhammadikram@gcu.edu.pk*

[d] *Core Research Facilities, King Fahd University of Petroleum & Minerals, Dhahran 31261, Saudi Arabia*

[e] *Nanomaterials Research Group (NRG), Physics Division, PINSTECH, Islamabad 44000, Pakistan*

Hence, efficient electrocatalysts are required to overcome these kinetic energy barriers.[22] Although Ir/Ru and Pt-based catalysts are esteemed for their performance in the OER and HER, the poor sustainability and high cost of such precious-metal-based catalysts significantly hinder their widespread applications.[23,24] Substantial efforts have been made in the pursuit of sustainable and economically viable electrocatalysts.[25] Transition metals, including transition metal dichalcogenides, oxides, and nitrides, have garnered considerable interest as promising alternative electrocatalysts.[26,27] MoS_2 is a widely studied TMDC, exhibiting unique properties, such as chemical inertness, large surface area, tunable interlayer spacing, and low toxicity. Owing to these excellent properties, MoS_2 has been broadly investigated as a co-catalyst in various catalytic processes, including dye elimination and hydrogen storage.[28,29] The structure of MoS_2 is composed of multiple monolayers, with Mo atoms sandwiched between two S atoms in each monolayer.[30] MoS_2 and Pt-based catalysts exhibit the same value of the Gibbs free energy for hydrogen adsorption ($\Delta G_H = 0$ eV), which makes them efficient electrocatalysts for HER.[31,32] In addition, the metallic (1T)-phase MoS_2 catalysts with enhanced intrinsic conductivity serve as optimum candidates in OER for delivering the lowest OER overpotentials, compared with the semiconducting (2H) phase.[33]

In general, pristine MoS_2 displays inadequate catalytic performance owing to insufficient exposed edge sites and relatively inactive basal planes.[34] There has been tremendous work done to increase the intrinsic catalytic performance of MoS_2, such as phase engineering, electrodeposition, and nanostructure engineering.[35] However, an effective approach is to facilitate electron transfer through the metallic doping of MoS_2.[36] In the previous studies, Group-V impurity elements, such as trivalent bismuth (Bi^{3+}), have been widely explored as ideal precursors for their non-toxic and inexpensive nature.[37] Additionally, silver (Ag) dopants are of immense interest for their unique physicochemical properties and large surface area, which is favorable for electrocatalytic processes.[38] The introduction of silver atoms into the MoS_2 lattice leads to the formation of new active sites and the enhancement of the electrocatalytic activity of MoS_2.[39,40]

The current study unveils the synergistic effect of Bi and Ag as dopants in the MoS_2 host, synthesized by an eco-friendly hydrothermal strategy. The resultant novel bifunctional Ag/Bi-doped MoS_2 heterogeneous catalyst displays exquisite catalytic degradation behavior against RhB dye and a remarkable electrocatalytic performance for OER.

2. Experimental details

2.1 Materials

$Na_2MoO_4 \cdot 2H_2O$ (99%), NH_2CSNH_2 (99.0%), $Bi(NO_3)_3 \cdot 5H_2O$ (98%), silver nitrate ($AgNO_3$, 90.0%), and HCl (37%) were procured from Sigma Aldrich, Germany.

2.2 Synthesis of the Ag/Bi-doped MoS_2

To prepare MoS_2 *via* the hydrothermal route, 0.5 M of $Na_2MoO_4 \cdot 2H_2O$ and 1 M of NH_2CSNH_2 were utilized as precursor materials, dissolved in deionized (DI) water and stirred at 60 °C for 15 min (Fig. 1a). The required amount of HCl was incorporated dropwise to sustain a pH of 2 for the stirred solution to obtain the precipitates. Subsequently, the precipitated solution was transported to a 100 mL autoclave at 180 °C for the completion of the reaction for 22 h. To eliminate the contaminants from the autoclaved solution, the colloidal solution was processed by centrifuging twice at 8000 rpm for 9 min and drying at 110 °C overnight to attain a fine powder (control sample). Furthermore, 2 wt% of $Bi(NO_3)_3 \cdot 5H_2O$ was integrated into the precursor solution of MoS_2 under the same environment to prepare Bi–MoS_2. Similarly, 1 and 3 wt% of $AgNO_3$ were

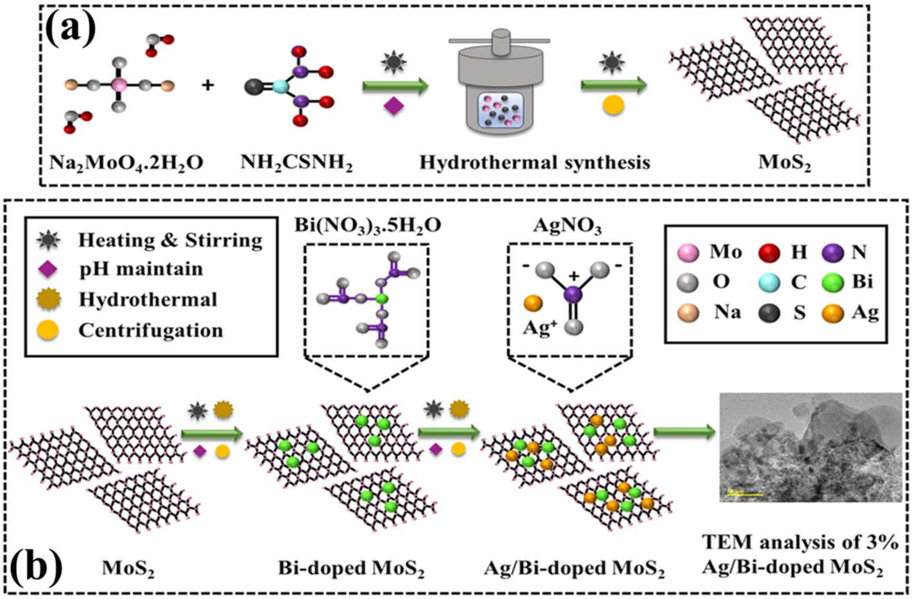

Fig. 1 Schematic of the synthesis of (a) MoS_2 and (b) Ag/Bi-doped MoS_2.

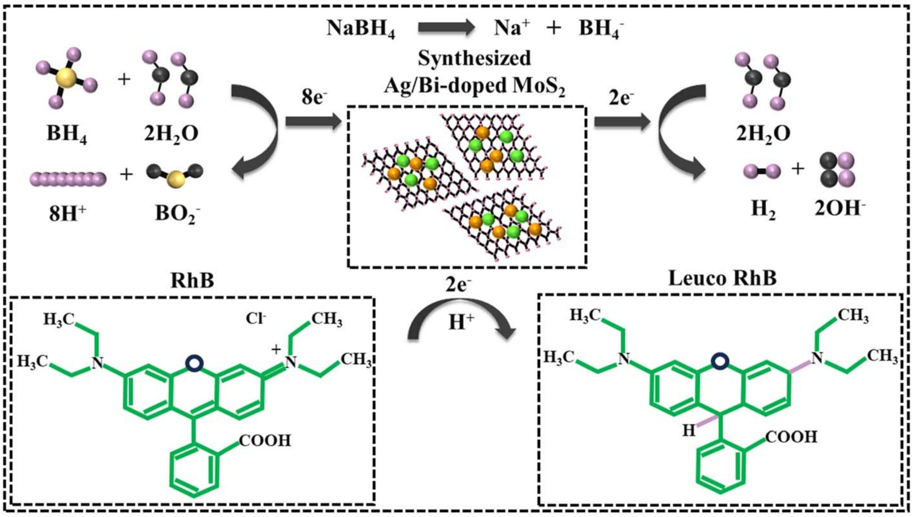

Fig. 2 Representation of the catalytic mechanism of Ag/Bi-doped MoS_2.

added to the binary system (precursor solution of Bi–MoS_2) to prepare Ag/Bi–MoS_2 (Fig. 1b).

2.3 Catalytic activity (CA)

The catalytic performances of MoS_2 and Ag/Bi-doped MoS_2 were determined by the breakdown of the RhB dye in the presence of a reducing agent ($NaBH_4$) in different pH environments (pH = 4, 12, 7) at room temperature. First, 400 μL of $NaBH_4$ was added to 3 mL of a RhB dye solution, followed by the incorporation of 400 μL of the (1, 3 wt%) Ag/Bi-doped MoS_2 synthesized samples. In the presence of the reducing agent, the synthesized samples (MoS_2 and Ag/Bi-doped MoS_2) were employed as catalysts for the reduction of the RhB dye. The degree of degradation was examined at regular intervals in the 200–800 nm range using a UV-Vis spectrophotometer. Incorporating $NaBH_4$ and the synthesized nanocatalysts resulted in the decolorization of the dye. The percentage degradation of the RhB dye was computed by the given eqn (1):

$$\%\ \text{Degradation} = C_0 - C_t/C_t \times 100. \tag{1}$$

Here, C_0 and C_t are the concentrations of the RhB dye at the beginning and end of the degradation procedure.

2.3.1 Mechanism of the catalytic activity. The mechanism of catalysis predominantly relies on two main factors: first, the incorporation of a reducing agent ($NaBH_4$) and second, the addition of newly synthesized nanocatalysts (Ag/Bi-doped MoS_2) into the RhB dye solution. The RhB dye is an oxidizing agent that gains an e^- from the reducing agent ($NaBH_4$) in a chemical reaction. In this process, an electron is transferred from a reductant to an oxidant, causing the breakdown of the synthetic dye. Generally, in the absence of catalysts, the redox reaction between $NaBH_4$ and RhB is slow. To increase the rate of redox reaction, nanocatalysts, such as MoS_2 and Ag/Bi-doped MoS_2, are incorporated into the redox reaction. These nanocatalysts reduce the activation energy required to initiate the reaction and serve as an electron transfer source between the reacting species, thereby facilitating the transfer of electron from BH_4^- (donor) to RhB^+ (acceptor) (Fig. 2). Furthermore, the synthesized catalyst's small size and large surface area provide a relatively high number of active sites for the adsorption of RhB and $NaBH_4$ onto catalyst's surface, resulting in the enhanced degradation of RhB.

2.4 Electrochemical measurements

A CS350M potentiostat was employed to analyze the OER performance of MoS_2, Bi–MoS_2, and 1%, 3% of Ag/Bi–MoS_2 using a Pt plate (counter electrode), catalyst slurry coated on Ni foam (working electrode, 308 mV overpotential of Ni-foam from our previous study 10.1002/adsu.202500317), and Ag/AgCl (reference electrode). The working electrode was prepared by the drop-wise coating of the synthesized sample slurry over the Ni foam. The slurry contained 4 mg of pristine and doped MoS_2 with 700 μL of ethanol and a few drops of Nafion. To obtain a homogeneous mixture, the slurry was sonicated for half an hour under ambient conditions. LSV was characterized at a sweep rate of 5 mV s^{-1} with a potential range of 1–2 V (*vs.* RHE). EIS was performed with 10 mV AC amplitude over a frequency range of 1 to 10^6 Hz.

3. Results and discussion

XRD patterns were obtained to scrutinize the crystal structure, phase purity and crystallographic planes of MoS_2 and Ag/Bi-doped MoS_2 within the 2θ range of 20–80° (Fig. 3a; 20 points smoothed). Diffraction peaks at 29.0° (006), 34.0° (012), 38.1° (104), 47.8° (107), 60.5° (1010), and 75.5° (1013) ascribed to rhombohedral phase of MoS_2 (JCPDS card# 01-077-0341). Peaks at 28.4° (102), 32.3° (202), 40.1° (112), and 56.6° (−205) revealed the monoclinic structure of $Mo_{2.06}S_3$ (JCPDS card# 01-072-0821). Additional peaks sited at 22.5° (201), 27.0° (114), 31.2° (122), 31.7° (106), and 45.° (134) assigned to hexagonal $Mo_{15}S_{19}$ phase (JCPDS card# 00-040-0936). Peak at 26.7° (411) correspond to monoclinic phase of sulphur (JCPDS card# 077-0228).[41] The

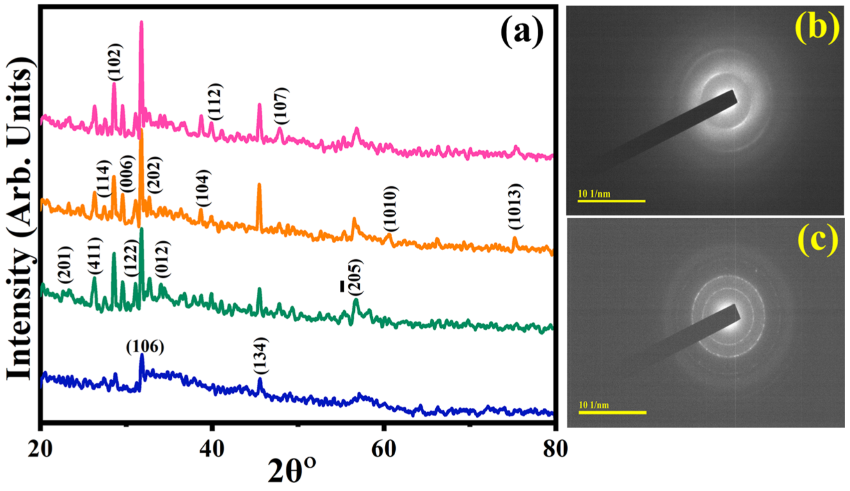

Fig. 3 (a) Diffraction patterns of MoS_2, Bi–MoS_2, 1% Ag/Bi-doped MoS_2, and 3% Ag/Bi-doped MoS_2 and (b and c) SAED analysis of Bi–MoS_2 and 3% Ag/Bi-doped MoS_2.

clear shift towards a relatively low 2θ value was observed after the doping with Bi, which was ascribed to the alteration of the lattice parameters in the MoS_2 host). Moreover, sharper peaks compared with those of pristine MoS_2 were revealed, which were associated with compressive stress during the growth of the crystallites.[42] The XRD patterns of the (1, 3 wt%) Ag/Bi-doped MoS_2 exhibited significantly intense diffraction peaks, signifying that the inclusion of Ag substantially improved the crystallinity of the sample.[43] The doping with silver slightly displaced the diffractogram towards a relatively small angle due to lattice distortion, modification of Bragg's condition and the exchange of Mo sites with Ag, which primarily was hindered by a large difference in the ionic radii of the host metal (Mo^{4+} = 0.59 Å) and dopant species (Ag^+ = 1.26 Å).[44–46] The calculated crystallite sizes of MoS_2, Bi–MoS_2, and 1%, 3% of Ag/Bi–MoS_2 were 91.37, 91.36, 59.92, and 60.90 nm, respectively. The relatively high density of grain boundaries due to the incorporation of Ag ions reduced the crystallite size by restricting the crystallite growth during nucleation. The presence of large ionic radii Ag ions potentially hindered grain growth and coarsening, pinning the grain boundaries and straining the host lattice.[44] Additionally, the SAED pattern illustrated bright rings, reflecting the polycrystalline nature of the Bi–MoS_2 and Ag/Bi-doped MoS_2, in accordance with the XRD patterns (Fig. 3b and c).

The optical properties of the pure, Bi–MoS_2 and Ag/Bi-doped MoS_2 were examined utilizing UV-vis absorption spectroscopy from 300–800 nm (Fig. 4a). The absorption peak of pristine MoS_2 was noticed within the wavelength range of 500–700 nm, with a maximum absorbance at 658 nm attributed to π–π^* transition.[47–50] Upon the doping of the host material with bismuth, the absorption window was enhanced. With the incorporation of silver in Bi–MoS_2, the absorption wavelength range was further increased, indicating an efficient charge transfer within the doped sample, resulting in the improved electrocatalytic performance of the Ag/Bi-doped MoS_2 catalyst.[51]

The FTIR analysis characterized the chemical structure of the MoS_2 and Ag/Bi-doped MoS_2 in the 4000–400 cm^{-1} range (Fig. 4b). The transmittance bands at 445, 491, and 603 cm^{-1} were attributed to the Mo–S stretching mode.[52–55] The incorporation of metal as a dopant affected the bands' intensities and their wavenumbers. The binding of the metal atoms with the host surface shifted the FTIR spectrum towards a relatively high

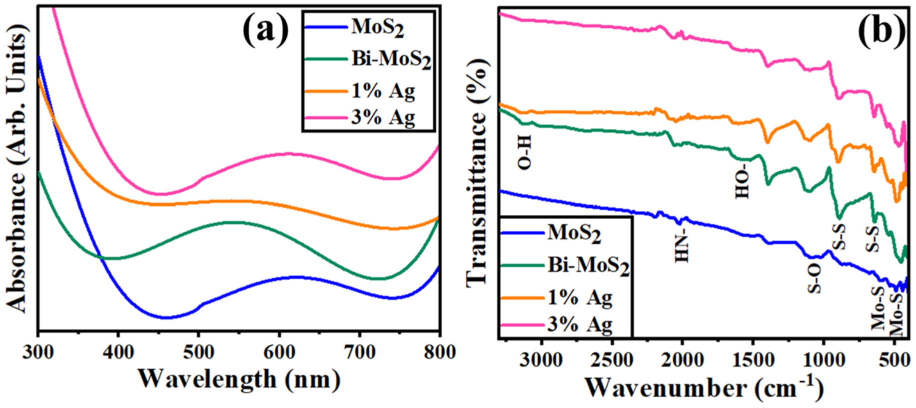

Fig. 4 (a) UV-vis spectra and (b) FTIR spectra of MoS_2, Bi–MoS_2, 1% Ag/Bi-doped MoS_2, and 3% Ag/Bi-doped MoS_2.

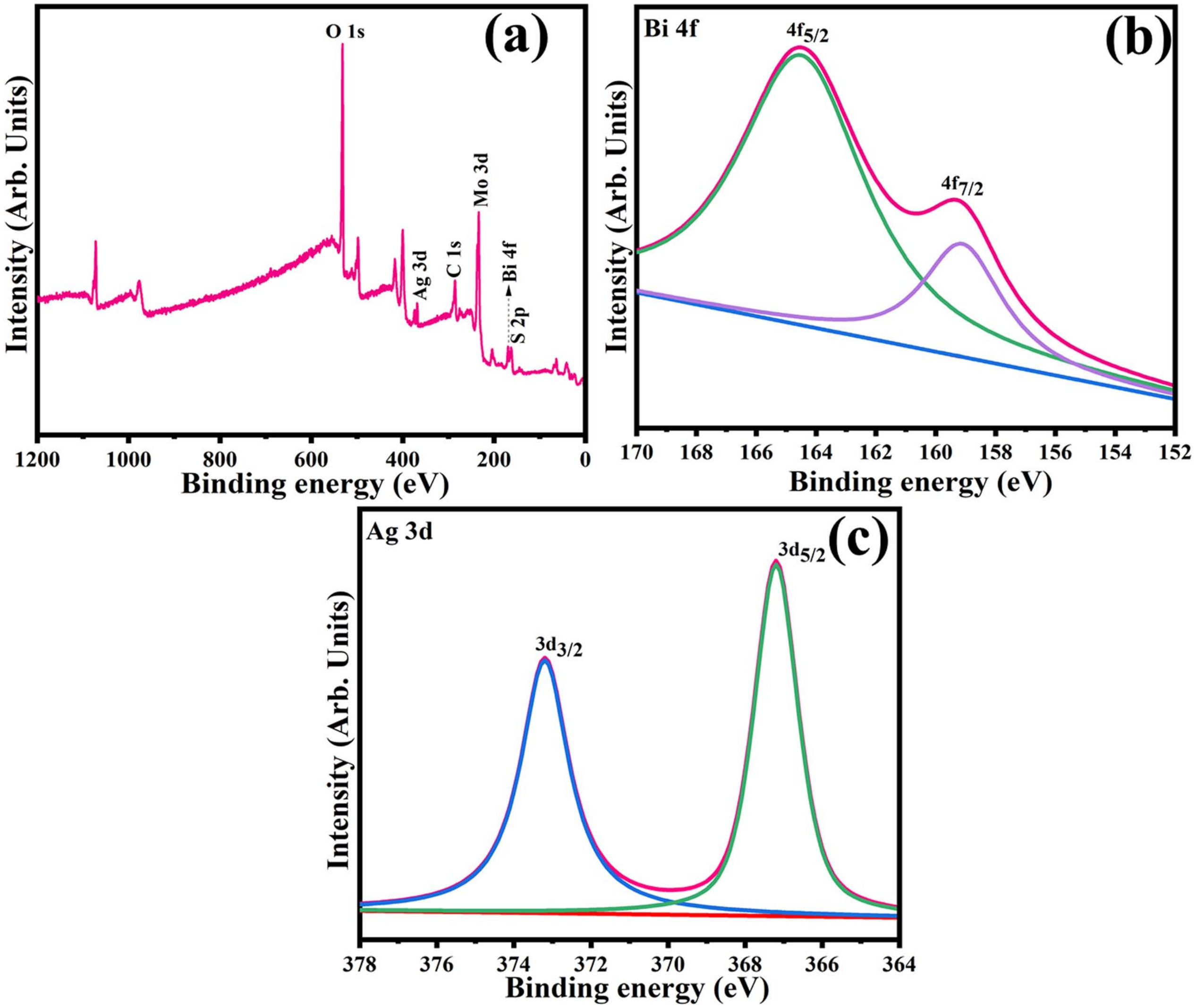

Fig. 5 (a) XPS survey spectrum of 3% Ag/Bi–MoS_2 and high-resolution spectra of (b) Bi 4f, and (c) Ag 3d.

wavenumber.[56] The band corresponding to the Mo–S vibration at 445 cm^{-1} for undoped MoS_2 shifted to 460 cm^{-1} for 2 wt% Bi and 472 cm^{-1} for 1 and 3 wt% Ag.[57] The bands at 644 and 894 cm^{-1} indicated the characteristic stretching mode of the S–S bond.[58,59] The band observed at 1104 cm^{-1} corresponded to the asymmetric S–O stretching mode.[60] The band at 1602 cm^{-1} was ascribed to the O–H bending vibrations of the absorbed water molecules.[61,62] The N–H stretching vibrations were accountable for the band at 2032 cm^{-1}.[63] The band at 3134 cm^{-1} appeared because of the O–H bond stretching vibration, which was related to intercalated water.[64]

To characterize the oxidation state of Ag/Bi–MoS_2, XPS analysis was utilized. The survey scan confirmed the existence of Mo, S, Bi, S, Ag, C and O (Fig. 5a). Mo 3d showed +4 and +6 oxidation states around 228, 232.5 and 235.8 eV, respectively.[65] S 2p revealed peaks at binding energies of 162.3 eV ($3d_{3/2}$) and 163.4 eV ($3d_{1/2}$) were observed.[66] The observed peaks at 159.6 and 165 eV in the Bi 4f spectrum were ascribed to $4f_{7/2}$ and $4f_{5/2}$ of Bi^{3+}, respectively (Fig. 5b).[67] The Ag 3d spectrum revealed peaks at 367.2 eV ($3d_{5/2}$) and 373.2 eV ($3d_{3/2}$), as shown in Fig. 5c.[68]

To elucidate the elemental composition of the control and doped MoS_2 samples, EDS measurements were performed. The prominent Mo and S peaks (Fig. S1a) reveal the successful preparation of MoS_2. The additional peaks of Bi and Ag (Fig. S1b–d) are attributed to the incorporation of the dopant species. The chlorine (Cl) peaks in the spectra arise from using HCl to maintain a pH of 2 during the preparation of the samples. Moreover, in order to minimize the charging effects, the specimens are usually sputter-coated with Au, inducing Au peaks in the spectrum. The EDS mapping of the as-synthesized highly doped MoS_2 sample was carried out to investigate the distribution of its elemental components, represented by distinct colors. The presence of various elements, Ag, Mo, and S, was confirmed (Fig. S2a–d).

FESEM analysis was implemented to examine the surface morphology and structure of MoS_2 and Ag/Bi-doped MoS_2. The pure sample exhibited agglomerated small-sized particles overlapped with the chunk, along with the random distribution of small and large clusters of particles (Fig. S3a). The doping of Bi into MoS_2 revealed the rod-shaped particles overlapped with the agglomerated non-uniform chunks (Fig. S3b).[69] With the incorporation of Ag (1 wt%), a flat rectangular rod-like morphology appeared with a few rod-shaped particles overlapping on the surface. Furthermore, the agglomeration of spherical-shaped particles was observed (Fig. S3c). Upon increasing the concentration of Ag (3 wt%), this pattern was increasingly revealed (Fig. S3d).

TEM micrographs were employed to investigate the morphological features and topography of MoS_2 and Ag/Bi-doped MoS_2. The formation of the wrinkled-nanosheets (NSs) of the pristine catalyst was revealed by TEM (Fig. 6a). The nanorod-shaped structures anchored in the NSs were observed because of the incorporation of Bi, confirming the interaction between Bi and MoS_2 NSs (Fig. 6b).[70] Upon the doping of Ag, a flat rectangular rod-like morphology was observed (Fig. 6c). The increased concentration of Ag revealed the agglomeration of distinct spherical, hexagonal, and rod-shaped nanoparticles distributed within the NSs. Furthermore, the aggregation of Ag nanoparticles resulted in the formation of a flat-lying nanoprism-like structure (Fig. 6d). The interlayer spacings of the pristine MoS_2, Bi–MoS_2, 1% Ag/Bi-doped MoS_2, and 3% Ag/Bi-doped MoS_2 were calculated from the HRTEM images using Gatan software and observed as 0.307, 0.312, 0.315, and 0.319 nm, respectively (Fig. S4a–d).

To assess the catalytic performance of the control and Ag/Bi-doped MoS_2 nanocatalysts against the RhB dye reduction using $NaBH_4$ in different pH environments, a UV-vis spectrophotometer was used. The degradation rates of pure and Ag/Bi-doped MoS_2 in an acidic medium (pH = 4) were 74.00%, 77.28%, 78.85%, and 82.71%; in a basic medium (pH = 12), 70.14%, 72.85%, 73.57%, and 80.00%; and in the neutral medium (pH = 7), 92.85%, 94.14%, 96.85%, and 99.57%, in 10 min (Fig. 7a–c). In comparison to the basic medium, both the acidic and neutral environments exhibited the highest RhB reduction. In the acidic medium, the high catalytic activity of the synthesized nanocatalyst was ascribed to the high concentration of H^+ ions for absorption on the surface of the catalyst. In the basic medium, the number of OH^- ions increased, resulting in the oxidation of the RhB dye and a decrease in the catalytic activity. Maximum reduction rates were examined in the neutral medium (pH = 7) for all catalysts; this might be due to the occurrence of the RhB dye in zwitterionic (RhB ±) and cationic (RhB^+) configurations in water.[71] Moreover, the doping of metal atoms in the host material played a significant role in catalysis. In the absence of dopants, the degradation efficiency of MoS_2 was relatively low in all media. When Bi (2 wt%) was doped in the MoS_2 lattice, it increased the surface area for absorption, leading to enhanced degradation efficiency. Likewise, the addition of Ag further improved the reductive degradation of dye by functioning as an e^- relay system and generating partially charged hydrogen species on the surface.[72,73] Upon increasing the concentration of Ag (3 wt%), the number of exposed active sites increased owing to the relatively small size of the Ag nanoparticles, resulting in the maximum breakdown of the RhB dye.[74] The MoS_2-based nanocatalyst offered the advantage of recycling to promote environmental sustainability practices. The effect of the recycled material on the dye degradation efficacy was determined by executing five cycles. The nanocatalysts were separated from the dye solution through centrifugation, dried and reused to run the next cycle of catalytic activity. At the end of each cycle, the degradation efficacy was determined, and the acquired outcomes are displayed in Fig. 7d. The as-synthesized nanocatalysts revealed high effectiveness towards recycling and reusability while sustaining their catalytic activities.

OER in an alkaline electrolyte is a complex four-electron process that involves a series of successive steps. It involves the formation of several intermediates like –OH, –O, and –OOH. The process begins with the formation of an M–OH intermediate, which is attributed to the adsorption of –OH at the metal

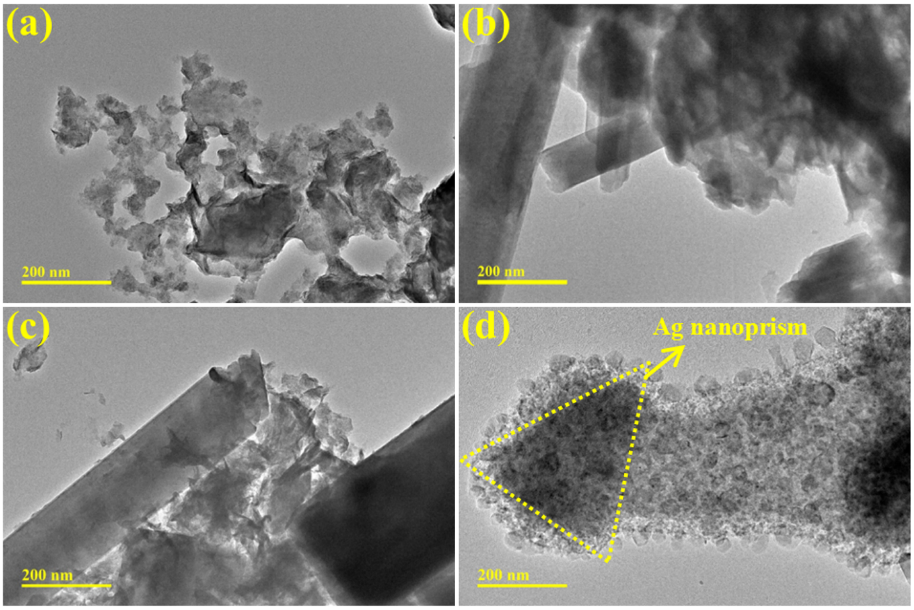

Fig. 6 TEM images of (a) MoS_2, (b) Bi–MoS_2, (c) 1% Ag/Bi-doped MoS_2, and (d) 3% Ag/Bi-doped MoS_2.

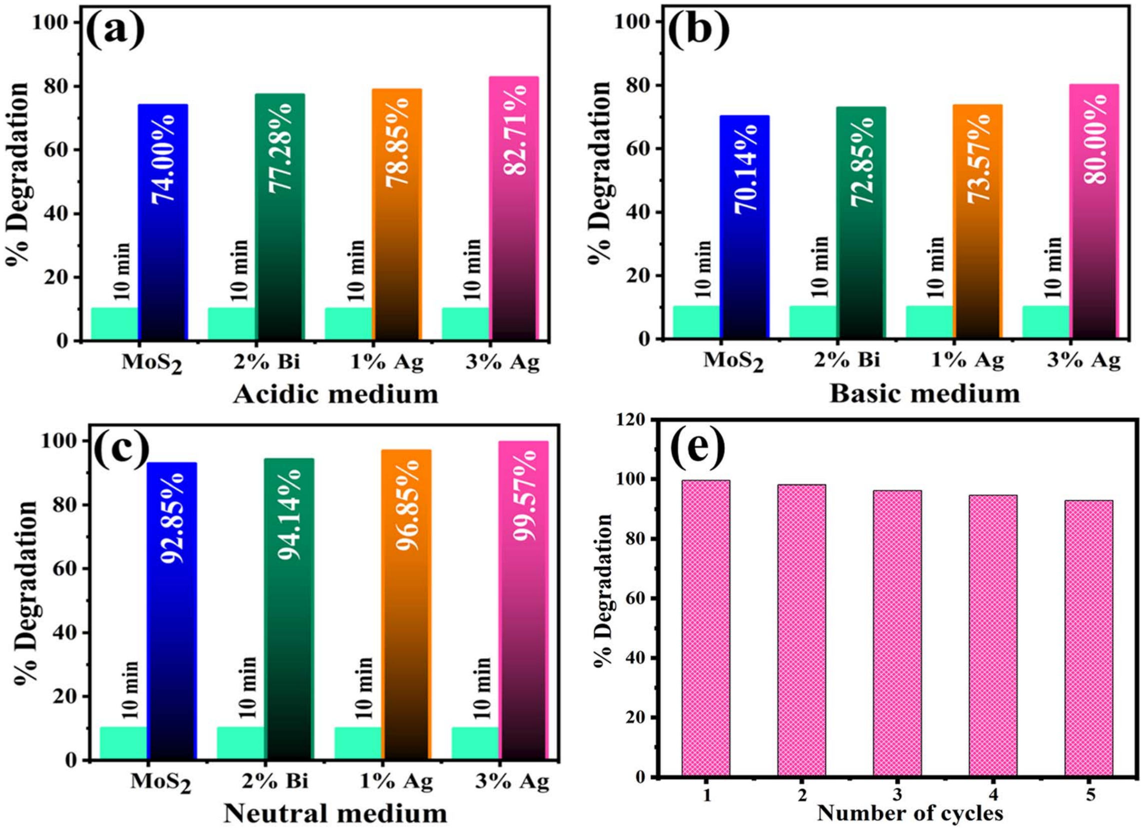

Fig. 7 Catalytic degradation of the RhB dye using MoS_2, Bi–MoS_2, 1% Ag/Bi-doped MoS_2, and 3% Ag/Bi-doped MoS_2 in (a) protonated, (b) basified, (c) neutral media, and (d) recycling experiments.

active site (M). The resulting M–OH further reacts with another –OH, generating an MO intermediate. The O_2 evolution steps are further divided into two possible categories, involving the generation of O_2 *via* the direct combinations of the MO intermediates and through the formation of MOOH that then generates M–O_2. The pathway that involves the formation of MOOH is less efficient and requires more energy, resulting in relatively slow reaction kinetics and low activity.[75–78]

The electrocatalytic activities of the MoS_2 and Ag/Bi-doped MoS_2 electrodes for OER were initially evaluated using the LSV curve. The LSV curves of the MoS_2, Bi–MoS_2, 1 wt% Ag/Bi-doped MoS_2, and 3 wt% Ag/Bi-doped MoS_2 electrodes are displayed (Fig. 8a). MoS_2 achieved the overpotential of 237 mV at 10 mA cm^{-2}, signifying the minimum catalytic performance of the pristine MoS_2 electrode. The overpotential of the Bi–MoS_2 electrode was 227 mV at constant current density, indicating that the incorporation of bismuth masked the edge active sites of MoS_2, resulting in decreased catalytic performance for OER compared with that of pristine MoS_2. However, the 1 wt% Ag/Bi-doped MoS_2 required the overpotential of only 224 mV to obtain a 10 mA cm^{-2} current response. In addition, the 3 wt% Ag/Bi-doped MoS_2 electrode demonstrated the lowest overpotential of 192 mV at the current density of 10 mA cm^{-2}, suggesting that the incorporation of Ag facilitates the OER kinetics of the electrode (Fig. 8b).[79] Consistent Tafel plots were calculated from the LSV polarization curves to further examine the insights into the OER kinetics. The Tafel slopes of MoS_2, Bi–MoS_2 and 1%, 3% Ag/Bi–MoS_2 were 118, 89.2, 108.9, and 65.3 mV dec^{-1}, respectively (Fig. 8c). The smallest Tafel plot value was obtained for the 3 wt% Ag/Bi-doped MoS_2 electrode, indicating its fastest OER kinetics owing to the increased concentration of Ag, which optimized the adsorption of hydroxyl radical ($OH^{\cdot}$) onto the catalyst's surface and lowered the kinetic energy barrier during OER.[80] The charge transfer properties of bifunctional Ag/Bi-doped MoS_2 electrodes were analyzed through EIS. The obtained Nyquist plots (Fig. 8d) revealed the largest semicircle diameter of the pristine MoS_2 electrode with the highest charge transfer resistance (R_{ct}), indicating the restricted diffusion of ions. The incorporation of Bi resulted in a decreased diameter of the semicircle, suggesting enhanced charge transfer and an accelerated rate of electrochemical reaction. The charge transfer resistance was significantly decreased for the 1 wt% Ag/Bi-doped MoS_2 electrode, owing to the resultant electronic interaction upon the inclusion of Ag. The smallest semicircle diameter in the Nyquist plots was observed for the 3 wt% Ag/Bi-doped MoS_2 electrode, implying the lowest charge transfer resistance, which was attributed to a relatively high concentration of Ag. This resulted in the maximum charge transfer at the electrode/electrolyte interface and a high current density, leading to favourable OER kinetics.[81,82] The comparison of the prepared electrocatalyst with other reported electrocatalysts is presented in Table S1.

The electrochemical performance of the electrocatalysts primarily depends on the intrinsic activity and active surface regions of the electrocatalysts, and it is usually determined by the

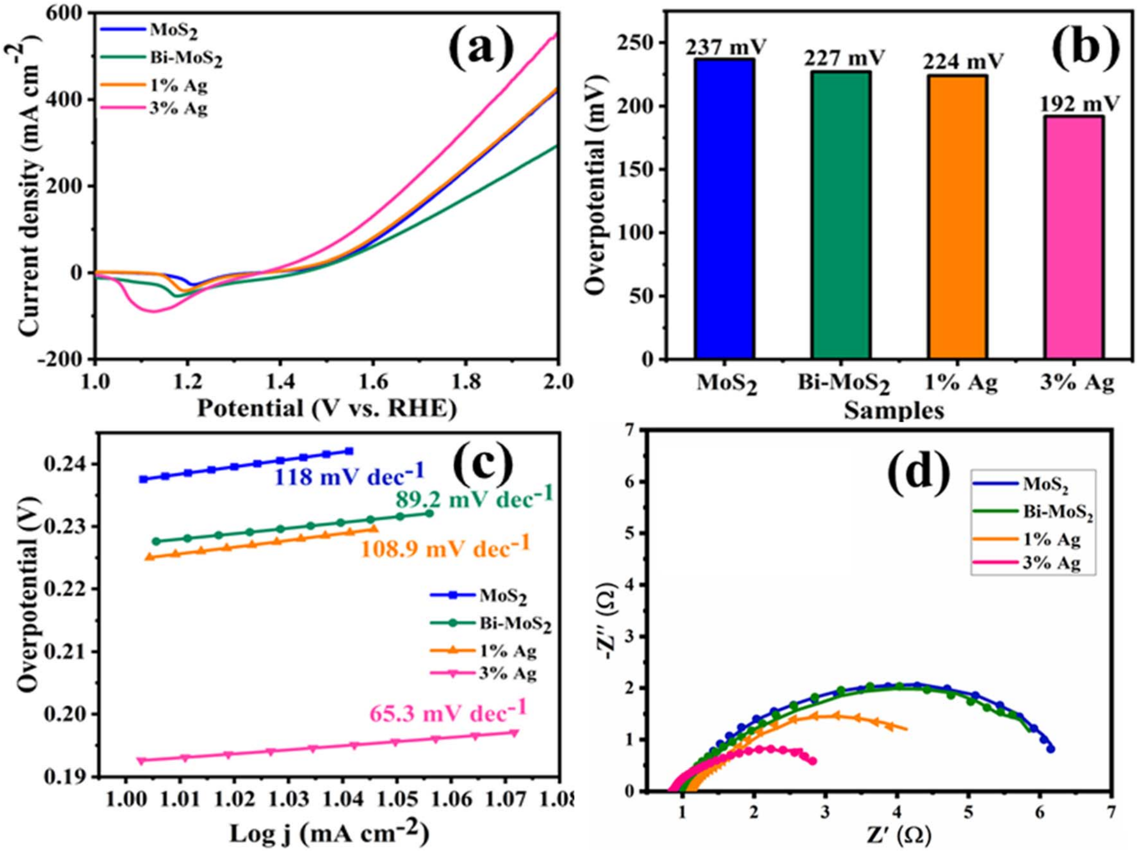

Fig. 8 (a) LSV polarization curves, (b) overpotentials at a current density of 10 mA cm^{-2}, (c) Tafel plots, and (d) EIS analysis of MoS$_2$, Bi–MoS$_2$, 1% Ag/Bi-doped MoS$_2$, and 3% Ag/Bi-doped MoS$_2$.

electrochemical active surface area (ECSA).[83] Relatively high values of ECSA demonstrate the existence of numerous exposed active surface areas, which are accountable for the excellent electrocatalytic behaviour of the electrode.[84] The ECSA is directly related to the C_{dl} value, estimated by testing CV curves at multiple scan rates. The C_{dl} values calculated for the MoS$_2$ and 3 wt% Ag/Bi-doped MoS$_2$ electrodes were 15.89 mF cm^{-2} and 19.55 mF cm^{-2}, respectively (Fig. S5). The significant increase in the ECSA results is attributed to the incorporation of 3 wt% Ag, suggesting the enhancement of active sites for efficient ion transfer, resulting in the exceptional OER activities of the electrocatalysts.

4. Conclusion

The present work demonstrates the synthesis of a novel bifunctional Ag/Bi-doped MoS$_2$ heterogeneous catalyst *via* a hydrothermal approach, with a fixed concentration (2 wt%) of Bi and varying concentrations (1 and 3 wt%) of Ag as dopants in the MoS$_2$ host. The synthesized catalyst was investigated for its catalytic properties in the degradation of RhB dye and its electrochemical OER performance. XRD patterns revealed the hexagonal structure of MoS$_2$. The elemental compositions of the control and doped MoS$_2$ samples were elucidated through EDS profiles. TEM analysis verified the formation of nanosheets (NSs) and nanorods, with a nanoprism-like structure observed with the increased concentration of Ag (3 wt%). The maximum catalytic activity of 99.57% for the elimination of the RhB dye was observed in the neutral medium in the presence of BH$_4^-$ ions. In the alkaline electrolyte, the 3 wt% Ag/Bi-doped MoS$_2$ electrode revealed outstanding electrocatalytic OER performance, requiring an overpotential of only 192 mV to reach a current density of 10 mA cm^{-2} and a small Tafel slope of 65.3 mV dec^{-1}. In conclusion, this study provides insights into the development of metal and non-metal-based catalysts for effective oxygen evolution and dye degradation.

Conflicts of interest

No conflict of interest.

Data availability

The data used in this manuscript can be available on reasonable request.

Supplementary information (SI) is available. See DOI: https://doi.org/10.1039/d5na00763a.

Acknowledgements

The authors are grateful to higher education commission (HEC) Pakistan for support through project NRPU-20-17615 (Muhammad Ikram, PI).

References

1 A. Issakhov, A. Alimbek and A. Abylkassymova, Numerical modeling of water pollution by products of chemical reactions from the activities of industrial facilities at variable and constant temperatures of the environment, *J. Contam. Hydrol.*, 2023, **252**, 104116.

2 R. Gusain, N. Kumar and S. S. Ray, Recent advances in carbon nanomaterial-based adsorbents for water purification, *Coord. Chem. Rev.*, 2020, **405**, 213111.

3 R. Waliullah, *et al.*, Optimization of toxic dye removal from contaminated water using chitosan-grafted novel nanocomposite adsorbent, *J. Mol. Liq.*, 2023, **388**, 122763.

4 R. H. Waghchaure, V. A. Adole and B. S. Jagdale, Photocatalytic degradation of methylene blue, rhodamine B, methyl orange and Eriochrome black T dyes by modified ZnO nanocatalysts: A concise review, *Inorg. Chem. Commun.*, 2022, **143**, 109764.

5 G. Bal and A. Thakur, Distinct approaches of removal of dyes from wastewater: A review, *Mater. Today: Proc.*, 2022, **50**, 1575–1579.

6 S. Kumar, *et al.*, N-doped ZnO–MoS_2 binary heterojunctions: the dual role of 2D MoS_2 in the enhancement of photostability and photocatalytic activity under visible light irradiation for tetracycline degradation, *Mater. Chem. Front.*, 2017, **1**(6), 1093–1106.

7 J. Wang and W. Azam, Natural resource scarcity, fossil fuel energy consumption, and total greenhouse gas emissions in top emitting countries, *Geosci. Front.*, 2024, **15**(2), 101757.

8 A. Farooq, *et al.*, Electrochemical investigation of C-doped $CoFe_2O_4/Fe_2O_3$ nanostructures for efficient electrochemical water splitting, *Int. J. Hydrogen Energy*, 2024, **51**, 1318–1332.

9 N. A. Khan, *et al.*, Boosting electrocatalytic hydrogen generation from water splitting with heterostructured $MoS_2/NiFe_2O_4$ composite in alkaline media, *Int. J. Hydrogen Energy*, 2024, **69**, 261–271.

10 T. Ren, *et al.*, Surface-sulphurated nickel–molybdenum alloy film as enhanced electrocatalysts for alkaline overall water splitting, *Int. J. Hydrogen Energy*, 2024, **57**, 983–989.

11 N. Ullah, *et al.*, In situ growth of M-MO (M= Ni, Co) in 3D graphene as a competent bifunctional electrocatalyst for OER and HER, *Electrochim. Acta*, 2019, **298**, 163–171.

12 A. Rebekah, *et al.*, Effect of cation substitution in $MnCo_2O_4$ spinel anchored over rGO for enhancing the electrocatalytic activity towards oxygen evolution reaction (OER), *Int. J. Hydrogen Energy*, 2020, **45**(11), 6391–6403.

13 C. Acar and I. Dincer, The potential role of hydrogen as a sustainable transportation fuel to combat global warming, *Int. J. Hydrogen Energy*, 2020, **45**(5), 3396–3406.

14 A. Grimm, *et al.*, Modeling photovoltaic-electrochemical water splitting devices for the production of hydrogen under real working conditions, *Int. J. Hydrogen Energy*, 2022, **47**(23), 11764–11777.

15 S. R. Qutb, *et al.*, Superior photoelectrodes of nanostructured Mo-doped CuO thin film for green hydrogen generation from photoelectrochemical water-splitting, *Int. J. Hydrogen Energy*, 2024, **76**, 190–201.

16 A. M. Shah, K. H. Modi, P. M. Pataniya, K. Simmy Joseph, S. Dabhi, G. R. Bhadu and C. K. Sumesh, Self-supported Mn-Ni_3Se_2 electrocatalysts for water and urea electrolysis for energy-saving hydrogen production, *ACS Appl. Mater. Interfaces*, 2024, **16**(9), 11440–11452.

17 C. Mohapatra, S. Ayushi, R. Sarma, A. Sharma, S. Singh Meena, P. M. Pataniya, C. K. Sumesh and N. K. Prasad, {Zr substituted (Fe3C/γ-Fe2O3)}@ C/NF as a High-Performance Electrocatalyst for Sustainable Water Splitting and H2 Production, *Ceram. Int.*, 2025, **51**(27), 52649–52661.

18 M. Sajid, *et al.*, Progress in the development of copper oxide-based materials for electrochemical water splitting, *Int. J. Hydrogen Energy*, 2024, **62**, 209–227.

19 K. B. Patel, *et al.*, Metal-organic framework derived core-shell nanoparticles as high performance bifunctional electrocatalysts for HER and OER, *Appl. Surf. Sci.*, 2023, **616**, 156499.

20 A. Farhan, *et al.*, Transition-metal sulfides with excellent hydrogen and oxygen reactions: A mini-review, *J. Solid State Chem.*, 2024, **329**, 124445.

21 A. Rajapriya, *et al.*, Enriched oxygen vacancy promoted heteroatoms (B, P, N, and S) doped CeO_2: Challenging electrocatalysts for oxygen evolution reaction (OER) in alkaline medium, *Int. J. Hydrogen Energy*, 2021, **46**(75), 37281–37293.

22 Y. Liu, *et al.*, A modulated electronic state strategy designed to integrate active HER and OER components as hybrid heterostructures for efficient overall water splitting, *Appl. Catal., B*, 2020, **260**, 118197.

23 T. Li and W. Hu, Ionic liquid derived electrocatalysts for electrochemical water splitting, *Green Energy Environ.*, 2024, **9**(4), 604–622.

24 B. Fang, *et al.*, Coordination regulated cobalt-based electrocatalysts for electrochemical water splitting, *Sep. Purif. Technol.*, 2024, **336**, 126188.

25 A. H. Al-Naggar, *et al.*, Water splitting performance of metal and non-metal-doped transition metal oxide electrocatalysts, *Coord. Chem. Rev.*, 2023, **474**, 214864.

26 H. Su, *et al.*, Recent progress on design and applications of transition metal chalcogenide-associated electrocatalysts for the overall water splitting, *Chin. J. Catal.*, 2023, **44**, 7–49.

27 N. A. Kamaruzaman, *et al.*, Recent advances in transition metals-based materials as electrocatalysts for water splitting, *Int. J. Electrochem. Sci.*, 2023, **18**(7), 100187.

28 Ritika, *et al.*, Rapid solar-light driven superior photocatalytic degradation of methylene blue using MoS_2-ZnO heterostructure nanorods photocatalyst, *Materials*, 2018, **11**(11), 2254.

29 F. Zhou, *et al.*, The electrochemical overall water splitting promoted by MoS_2 in coupled nickel–iron (oxy) hydride/molybdenum sulfide/graphene composite, *Chem. Eng. J.*, 2020, **397**, 125454.

30 H. Fei, *et al.*, Extending MoS_2-based materials into the catalysis of non-acidic hydrogen evolution: challenges,

progress, and perspectives, *Mater. Futures*, 2023, **2**(2), 022103.

31 S. Geng, *et al.*, Activating interfacial S sites of MoS_2 boosts hydrogen evolution electrocatalysis, *Nano Res.*, 2022, 1–8.

32 D. Han, *et al.*, Synergistic engineering of MoS_2 via dual-metal doping strategy towards hydrogen evolution reaction, *Appl. Surf. Sci.*, 2020, **529**, 147117.

33 F. Gong, *et al.*, Boosting electrochemical oxygen evolution over yolk-shell structured O–MoS_2 nanoreactors with sulfur vacancy and decorated Pt nanoparticles, *Nano Energy*, 2020, **78**, 105284.

34 Z. Hong, *et al.*, Stable 1T–2H MoS_2 heterostructures for efficient electrocatalytic hydrogen evolution, *Chem. Eng. J.*, 2023, **460**, 141858.

35 X. Zhang and Y. Liang, Nickel hydr (oxy) oxide nanoparticles on metallic MoS_2 nanosheets: a synergistic electrocatalyst for hydrogen evolution reaction, *Adv. Sci.*, 2018, **5**(2), 1700644.

36 X. Chen, *et al.*, Enhanced hydrogen evolution reaction performance of MoS_2 by dual metal atoms doping, *Int. J. Hydrogen Energy*, 2022, **47**(55), 23191–23200.

37 B. E. Nagay, *et al.*, Visible-light-induced photocatalytic and antibacterial activity of TiO_2 codoped with nitrogen and bismuth: new perspectives to control implant-biofilm-related diseases, *ACS Appl. Mater. Interfaces*, 2019, **11**(20), 18186–18202.

38 A. A. I. Khalil, A.-S. H. Abd El-Gawad and A.-S. Gadallah, Impact of silver dopants on structural, morphological, optical, and electrical properties of copper-zinc sulfide thin films prepared via sol-gel spin coating method, *Opt. Mater.*, 2020, **109**, 110250.

39 A. Nazneen, *et al.*, Structural, morphological, optical, and photocatalytic properties of Ag-doped MoS_2 nanoparticles, *J. Mol. Struct.*, 2020, **1220**, 128735.

40 D. Vikraman, *et al.*, Engineering the active sites tuned MoS_2 nanoarray structures by transition metal doping for hydrogen evolution and supercapacitor applications, *J. Alloys Compd.*, 2022, **893**, 162271.

41 U. Qumar, *et al.*, Synergistic effect of Bi-doped exfoliated MoS_2 nanosheets on their bactericidal and dye degradation potential, *Dalton Trans.*, 2020, **49**(16), 5362–5377.

42 A. H. C. Khavar, A. R. Mahjoub and S. Najafi, Enhanced photocatalytic degradation of tetracycline by improving electron flux at the Schottky junction between Bi nanoparticles and MoS_2-anchored RGO, *J. Photochem. Photobiol., A*, 2024, **447**, 115270.

43 S. G. TC, Genuine two-photon absorption and optical limiting property of the Ag–rGO–MoS_2 hybrid: implications for laser safety devices, *ACS Appl. Nano Mater.*, 2024, **7**(4), 3885–3896.

44 S. M. Al Amin and M. A. Kowser, Influence of Ag doping on structural, morphological, and optical characteristics of sol-gel spin-coated TiO_2 thin films, *Heliyon*, 2024, **10**(18), e37558.

45 M. Aldrdery, *et al.*, Rare earth metal doped molybdenum sulfide microflowers reinforced with graphene for the photocatalytic annihilation of ciprofloxacin drug, *Diamond Relat. Mater.*, 2025, **153**, 112072.

46 S. S. Wagh, *et al.*, Comparative studies on synthesis, characterization and photocatalytic activity of Ag doped ZnO nanoparticles, *ACS Omega*, 2023, **8**(8), 7779–7790.

47 V. Forsberg, *et al.*, Exfoliated MoS_2 in water without additives, *PloS One*, 2016, **11**(4), e0154522.

48 A. A. E.-F. Abdulaziz, *et al.*, One-step hydrothermal synthesis of 2H-MoS_2 nanoflowers for efficient degradation of methylene blue and rhodamine B dyes under UV and visible-light irradiation: A comparative study, *Assiut Univ. J. of Multidisciplinary Sci. Res.*, 2024, **53**(2), 308–334.

49 M. El-Nahass, K. Abd-El-Rahman and A. Darwish, Fourier-transform infrared and UV–vis spectroscopes of nickel phthalocyanine thin films, *Mater. Chem. Phys.*, 2005, **92**(1), 185–189.

50 B. Manoj and A. Kunjomana, Analytical Study of Two Differently Ranked Coals Using UV-VIS-NIR Spectroscopy, *J. Miner. Mater. Charact. Eng.*, 2011, **10**(10), 905–911.

51 T. Yang, *et al.*, Designed bifunctional flower-like structural molybdenum disulfide doped with Ag atoms for clean energy and contaminant detection, *Int. J. Hydrogen Energy*, 2024, **51**, 703–712.

52 K. Peng, *et al.*, Hierarchical MoS_2 intercalated clay hybrid nanosheets with enhanced catalytic activity, *Nano Res.*, 2017, **10**, 570–583.

53 N. Kumar, *et al.*, Probing on crystallographic structural and surface morphology of hydrothermally synthesized MoS_2 nanoflowers consisting of nanosheets, *Appl. Surf. Sci. Adv.*, 2021, **6**, 100167.

54 S. Karade, D. Dubal and B. Sankapal, MoS_2 ultrathin nanoflakes for high performance supercapacitors: room temperature chemical bath deposition (CBD), *RSC Adv.*, 2016, **6**, 39159–39165.

55 S. Kumar, *et al.*, Pyrene-based 2D covalent organic framework engineered with 3D-MoS_2-nanoflowers tuned with high surface area assisted in visible-light-driven photocatalytic H2 evolution and CO2 reduction, *ACS Appl. Energy Mater.*, 2024, **7**(10), 4429–4444.

56 M. E. M. Ali, *et al.*, Green MoS_2 nanosheets as a promising material for decontamination of hexavalent chromium, pharmaceuticals, and microbial pathogen disinfection: spectroscopic study, *J. Nanopart. Res.*, 2022, **24**(10), 191.

57 S. Saleem, *et al.*, Electrocatalytic hydrogen evolution reaction on sulfur-deficient MoS_2 nanostructures, *Int. J. Hydrogen Energy*, 2022, **47**(12), 7713–7723.

58 N. Hussain, *et al.*, Cu2O nanoparticles decorated with MoS_2 sheets for electrochemical reduction of CO_2 with enhanced efficiency, *Appl. Phys. A*, 2022, **128**(2), 131.

59 S. P. Vattikuti and C. Byon, Synthesis and characterization of molybdenum disulfide nanoflowers and nanosheets: nanotribology, *J. Nanomater.*, 2015, **2015**(1), 710462.

60 M. R. Charapale, *et al.*, Hierarchical 3D flowers of 1T@ 2H-MoS_2 assembled with an array of ultrathin nano-petals for high-performance supercapacitor electrodes, *J. Solid State Electrochem.*, 2024, **28**(1), 181–195.

61 G. A. Ali, *et al.*, One-step electrochemical synthesis of MoS_2/graphene composite for supercapacitor application, *J. Solid State Electrochem.*, 2020, **24**, 25–34.

62 P. Sharma, *et al.*, Unveiling Xanthine Presence in Rohu Fish Using Ag+-Doped MoS_2 Nanosheets Through Electrochemical Analysis, *Appl. Biochem. Biotechnol.*, 2024, **196**(8), 5219–5234.

63 J. Jang, *et al.*, MoS_2-cysteine nanofiltration membrane for lead removal, *ChemEngineering*, 2021, **5**(3), 41.

64 R. Rahman, *et al.*, Tuning of structural and optical properties with enhanced catalytic activity in chemically synthesized Co-doped MoS_2 nanosheets, *RSC Adv.*, 2021, **11**(3), 1303–1319.

65 X. Zhang, *et al.*, Green Synthesis of Flowerball-like MoS_2/VC Nanocomposite and Its Efficient Catalytic Performance for Oxygen Reduction Either in Alkaline or Acid Media, *Catalysts*, 2022, **12**(3), 259.

66 B. Lai, *et al.*, Hydrogen evolution reaction from bare and surface-functionalized few-layered MoS_2 nanosheets in acidic and alkaline electrolytes, *Mater. Today Chem.*, 2019, **14**, 100207.

67 S. Li, *et al.*, Nitrogen-doped bismuth nanosheet as an efficient electrocatalyst to CO_2 reduction for production of formate, *Int. J. Mol. Sci.*, 2022, **23**(22), 14485.

68 S. V. Singh, *et al.*, Direct evidence of an efficient plasmon-induced hot-electron transfer at an in situ grown Ag/TiO_2 interface for highly enhanced solar H_2 generation, *ACS Appl. Energy Mater.*, 2020, **3**(2), 1821–1830.

69 Z. Li, *et al.*, Role of bismuth doping on structural and electrical properties of Zno nanocrystals prepared by sol–gel method, *J. Electron. Mater.*, 2024, **53**(5), 2504–2513.

70 M.-C. Wu, J.-S. Chih and W.-K. Huang, Bismuth doping effect on TiO_2 nanofibres for morphological change and photocatalytic performance, *CrystEngComm*, 2014, **16**(46), 10692–10699.

71 E. U. Haq, *et al.*, Catalytic action and bactericidal behavior of samarium/carbon spheres-doped manganese oxide nanostructures and their molecular docking analysis, *J. Alloys Compd.*, 2024, **973**, 172760.

72 B. Vellaichamy and P. Periakaruppan, Ag nanoshell catalyzed dedying of industrial effluents, *RSC Adv.*, 2016, **6**(38), 31653–31660.

73 M. R. Pradhan, *et al.*, Enhanced catalytic reductive hydrogenation of an organic dye by Ag decorated graphitic carbon nitride modified MCM-41, *RSC Adv.*, 2024, **14**(2), 1072–1081.

74 M. T. Ameen, *et al.*, Exploring catalytic efficacy and anti-bacterial performance with molecular docking analysis of g-C3N4-grafted-Ag doped SnO_2 QDs, *Res. Chem. Intermed.*, 2024, **50**(4), 1661–1678.

75 J. Joo, *et al.*, Morphology-controlled metal sulfides and phosphides for electrochemical water splitting, *Adv. Mater.*, 2019, **31**(14), 1806682.

76 R. He, X. Huang and L. Feng, Recent progress in transition-metal sulfide catalyst regulation for improved oxygen evolution reaction, *Energy Fuels*, 2022, **36**(13), 6675–6694.

77 B. Chen, *et al.*, In situ porousized MoS2 nano islands enhance HER/OER bifunctional electrocatalysis, *Small*, 2023, **19**(14), 2207177.

78 G. Srividhya, *et al.*, Cobalt–iron co-substituted NiV layered double hydroxide as a high-performance electrocatalyst for oxygen evolution reaction in a neutral saline medium, *ACS Appl. Energy Mater.*, 2023, **7**(1), 154–164.

79 T. Yu, *et al.*, Ag improves the performance of the oxygen evolution reaction by lowering the D-band center of the active site Ni, *Int. J. Hydrogen Energy*, 2024, **51**, 935–944.

80 G. Solomon, *et al.*, Decorating vertically aligned MoS_2 nanoflakes with silver nanoparticles for inducing a bifunctional electrocatalyst towards oxygen evolution and oxygen reduction reaction, *Nano Energy*, 2021, **81**, 105664.

81 B. J. Rani, *et al.*, Fabrication and electrochemical OER activity of Ag doped MoO_3 nanorods, *Mater. Sci. Semicond. Process.*, 2020, **107**, 104818.

82 A. M. Tighezza, *et al.*, Fabrication of excellent and novel flowery Ag-MoS_2 electrocatalyst: As a high-efficiency for water oxidation, *Mater. Res. Bull.*, 2025, **184**, 113262.

83 D. Han, *et al.*, Activating MoS_2 via electronic structure modulation and phase engineering for hydrogen evolution reaction, *Catal. Commun.*, 2022, **164**, 106427.

84 N. Rasool, *et al.*, Enhancement of $BaCeO_3$ OER performance by generating a nanohybrid with gCN for electrochemical water splitting, *Int. J. Hydrogen Energy*, 2024, **81**, 562–572.